Geophysical Journal International

Geophys. J. Int. (2012) **188,** 994–1006 doi: 10.1111/j.1365-246X.2011.05317.x

Constraining ice mass loss from Jakobshavn Isbræ (Greenland) using InSAR-measured crustal uplift

Lin Liu,[1]★ John Wahr,[1] Ian Howat,[2] Shfaqat Abbas Khan,[3] Ian Joughin[4] and Masato Furuya[5]

[1]*Department of Physics and Cooperative Institute for Research in Environmental Sciences, University of Colorado, Boulder, CO, USA. E-mail: liulin@stanford.edu*
[2]*Byrd Polar Research Center, School of Earth Sciences, Ohio State University, Columbus, OH, USA*
[3]*DTU Space - National Space Institute, Department of Geodesy,* 2100 *Copenhagen Ø, Denmark*
[4]*Applied Physics Laboratory, Polar Science Center, University of Washington, Seattle, WA, USA*
[5]*Department of Natural History Sciences, Hokkaido University, Sapporo, Japan*

Accepted 2011 November 24. Received 2011 June 16; in original form 2010 May 6

SUMMARY

Jakobshavn Isbræ in west Greenland has been undergoing dramatic thinning since 1997. Applying the interferometric synthetic aperture radar (InSAR) technique to Radarsat-1 SAR data, we measure crustal uplift near Jakobshavn Isbræ caused by recent ice mass loss. The crustal uplift is predominantly at long spatial wavelengths (larger than 10 km), and thus is difficult to separate from InSAR orbit errors. We reduce the effects of orbit errors by removing long-wavelength deformation signals using conventional InSAR baseline fitting methods. We find good agreement between the remaining short-scale InSAR-estimated deformation rates during 2004–2008 and the corresponding short-scale components of a deformation model that is based on changes in ice elevation measured by NASA's Airborne Topographic Mapper (ATM). We are also able to use the InSAR-measured deformation to invert for the spatial pattern of ice thinning. Overall, our results suggest that despite the inherent difficulties of working with a signal that has significant large-scale components, InSAR-measured crustal deformation can be used to study the ice mass loss of a rapidly thinning glacier and its surrounding catchment, providing both a constraint on any existing model of ice mass loss and a data source that can be used to invert for ice mass loss. These new applications of InSAR can help to better understand a glacier's rapid response to a warming climate.

Key words: Space geodetic surveys; Radar interferometry; Glaciology; Kinematics of crustal and mantle deformation; Arctic region.

1 INTRODUCTION

Jakobshavn Isbræ, the largest outlet glacier on Greenland's west coast, has been undergoing substantial thinning in ice elevation for more than a decade. Since 1991, NASA Wallops Flight Facility has conducted annual repeat laser altimetry surveys over Jakobshavn Isbræ along a grid pattern of flight tracks using the Airborne Topographic Mapper (ATM, Krabill *et al.* 1999, 2000; Thomas *et al.* 2003; Krabill *et al.* 2004; Joughin *et al.* 2008; Thomas *et al.* 2009). These surveys reveal a progressive loss of ice volume from the glacier, from $\sim$10 km^3 yr^{-1} during 1997–2002, to $\sim$20 km^3 yr^{-1} during 2002–2003 (Krabill *et al.* 2004), to $\sim$23 km^3 yr^{-1} during 2005–2006 (Joughin *et al.* 2008) and a slight decrease to $\sim$22 km^3 yr^{-1} during 2006–2009 (Khan *et al.* 2010a).

Because of their high spatial resolution, ATM surveys provide one of the best data sets for estimating the mass balance from individual glaciers. However, their accuracy is mainly limited by two factors. First, repeat survey tracks only cover a portion of the Jakobshavn Isbræ drainage basin, excluding some of its inland area. Therefore, a regional synopsis requires spatial interpolation and extrapolation of the survey grids, which introduce uncertainties in total mass balance estimates. Secondly, a surface snow/ice density profile is required to convert changes in glacier elevation into mass changes. However, surface density can only be reliably determined from field measurements (Cuffey & Paterson 2010), which are infrequent and sparse at Greenland glaciers. A constant vertical-averaged density, for example, density of pure ice of 910 kg m^{-3} (Joughin *et al.* 2008), is usually used. Under this assumption, the estimated rate

★Now at: Department of Geophysics, Stanford University, Stanford, CA, USA.

of ice volume loss could be biased by the temporal and spatial variability of the surface mass balance (SMB). Though, depending on the time of year, the assumption of a uniform ice density might be appropriate for Jakobshavn Isbræ, because most of its mass loss occurs in the ablation zone.

As a complement to altimetry studies, GPS-measured crustal deformation is useful for constraining estimates of present-day ice mass balance (Sauber & Molnia 2004; Dietrich *et al.* 2005; Khan *et al.* 2007; Bevis *et al.* 2009; Kierulf *et al.* 2009; Khan *et al.* 2010a,b; Dietrich *et al.* 2010). The Earth's crust deforms elastically in response to present-day unloading of ice from a thinning glacier. Khan *et al.* (2010a) analysed data from continuous GPS measurements on bedrock near Jakobshavn Isbræ and found that all four sites showed clear uplifting trends during 2006–2009. A large uplift rate of $14.6 \pm 1.7\,\mathrm{mm\,yr^{-1}}$ was observed at Kangia, located immediately adjacent to the glacier front, in response to glacial thinning (Khan *et al.* 2010a). GPS measurements have the advantages of being sensitive to mass rather than to elevations, and of inherently averaging over large spatial regions without the risk of missing an area of significant mass change. A disadvantage is that a handful of GPS receivers in a region does not provide a high-resolution deformation field.

The main goal of this study is to constrain Jakobshavn Isbræ ice mass balance estimates using glacial-unloading deformation over the adjacent bedrock, as measured by interferometric synthetic aperture radar (InSAR). We demonstrate that the InSAR measurements can be used in two ways. First, we compare InSAR-measured deformation with the deformation predicted from the ATM data. Because InSAR provides an assessment of the deformation across an entire region rather than at just a few points, it can in principle provide a better constraint on the ice mass balance than GPS. Secondly, we invert for ice thinning rates at a relatively high spatial resolution (5 km), using the complete InSAR regional deformation measurements. We conclude that such inversions can provide a direct means of studying ice mass balance even when no other data are available directly over the ice. Overall, these two new applications extend conventional InSAR studies on mapping glacial motions to constrain mass balance.

InSAR has been widely applied to measure surface velocities of glaciers (Goldstein *et al.* 1993; Joughin *et al.* 1996; Rignot *et al.* 1997; Joughin 2002; Joughin *et al.* 2004; Rignot & Kanagaratnam 2006), but not, to our knowledge, to measure unloading deformation caused by glacial mass loss, mainly because long-wavelength deformation is difficult to distinguish from InSAR orbit errors. That is the major technical challenge in this work, and part of our goal is to explore the limitations introduced by those errors.

2 CRUSTAL DEFORMATION MODEL BASED ON THE ATM SURVEYS

We use the ATM data to model the crustal deformation rate in response to glacial thinning during the time span of the SAR scenes. This model will be used in Section 3 to compare with the InSAR measurements.

We differentiate successive ATM surveys in the summers of 1997, 2002, 2005, 2006 and 2009, and resample the flight track elevation changes onto a 1 km grid (Joughin *et al.* 2008). The resulting maps of surface elevation change (Fig. 2) show dramatic ice thinning in the glacier trunk, as well as interannual variability. The thinning rate increased steadily near the ice front and reached 10–30 m yr^{-1} during 2005–2006, then decreased to $\sim$12 m yr^{-1} during 2006–2009, consistent with the gradual migration of thinning upglacier towards the inland ice. The grounding line (shown as the red line in Fig. 1) remained relatively stable during the 2004–2008 InSAR time span (Khan *et al.* 2010a).

At an InSAR pixel i, the line-of-sight (LOS) deformation rate, d_i, in response to thinning from N discrete ice mass points can be written as

$$d_i = \sum_{j=1}^{N} g_{i,j} u_j, \tag{1}$$

where $g_{i,j}$ is the loading deformation Green's function (Farrell 1972) projected into the LOS direction, and u_j is the ice thinning rate determined from changes in surface elevation from ATM surveys. The ATM-derived ice thinning rates also include contributions from the elastic uplift of the bed. However, since those contributions are only about 1 per cent of the ice thinning, their impact on our estimates of d_i is negligible.

At each pixel, we calculate the deformation rates during 2004–2008. In Fig. 3, we only plot predictions at points displaying high coherence in the Radarsat-1 interferograms. Most of these points are located on bedrock, as interferograms lose coherence over the glacier and water bodies. The LOS motion is dominated by vertical motion, with horizontal motion contributing less than 5 per cent. LOS shortening (nearly uplift) is largest near the glacier, with a maximum rate of 12 mm yr^{-1}. Shortening rates decrease at distances further from the glacier. This spatial pattern resembles a tilt with high gradients near the glacier and with a nearly constant gradient on the west side.

In addition to the ice mass loss from Jakobshavn Isbræ, three other sources also contribute to the InSAR-measured crustal deformation, all of which we model and remove from the interferograms. The first is loading from ice-dammed Tiningnilik Lake, located south of Jakobshavn Icefjord (Fig. 1). After a rapid draining episode in 2003, the lake's water level has been rising at an estimated rate of 7.5 m yr^{-1} (Furuya & Wahr 2005), which has caused ground subsidence around the lake. The calculated elastic crustal deformation shows a localized lobe pattern of LOS lengthening, at rates up to 2.0 mm yr^{-1}. The second is the Earth's viscoelastic response to the deglaciation history since the last glacial maximum. We spatially interpolate the 3-D present-day post-glacial rebound (PGR) rates given by the ICE-5G model of Peltier (2004), and project them into the LOS direction. The predicted PGR signal resembles a slope with LOS lengthening (nearly subsidence) rates, which decrease from 1.6 mm yr^{-1} in the east to 0.4 mm yr^{-1} in the west. The third is the ocean tide loading (OTL) deformation over this coastal area. Following the method of DiCaprio & Simons (2008), we model the OTL deformation for the individual interferograms using the NLOADF program (Agnew 1997) and the GOT00.2 ocean tide model (Ray 1999). We find a maximum spatial gradient in OTL of 1 cm across any interferogram (50 km wide). Nonetheless, the apparent linear rate of OTL calculated using the time-series sampled by our 36 SAR acquisition times is less than 0.8 mm yr^{-1} and varies by only 0.2 mm yr^{-1} across the InSAR frame.

After constructing the model of the LOS rates, we simulate the surface deformation fields (hereafter referred to as 'synthetic interferograms') corresponding to the real interferograms by multiplying the predicted linear rates by the time intervals of the individual interferograms. Each synthetic interferogram and its corresponding Radarsat-1 interferogram share the same orbital information.

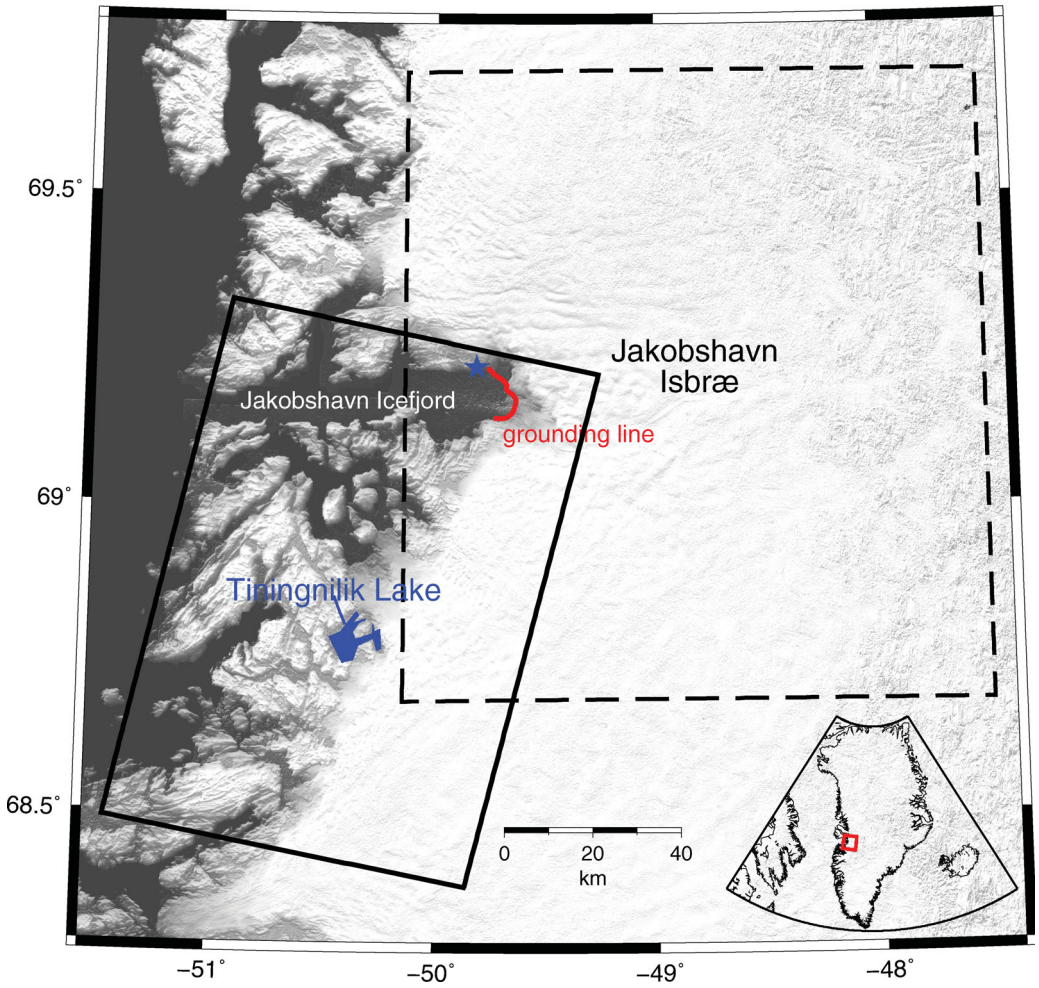

Figure 1. Map of Jakobshavn Isbræ and the adjacent bedrock. The background image is topographic relief. The solid black box outlines the coverage of the Radarsat-1 SAR scenes. The dashed box outlines the boundary of the glacial thinning models constructed from the ATM altimetry surveys, which are shown in Fig. 2. The red curve is the grounding line. The red box in the inset map shows the location of the study area.

3 InSAR PROCESSING AND RESULTS

3.1 Overview

We use fine-beam (beam F1) SAR data collected by Radarsat-1, a Canadian Space Agency (CSA) satellite. The Radarsat-1 SAR scenes (listed in Table 1) spanned 2004–2008, when the glacier was progressively losing ice (Joughin *et al.* 2008). We concatenate two adjacent SAR frames (frames 277 and 278, shown in Fig. 1) for full coverage over the bedrock area close to the glacier and for better estimation of InSAR orbit errors (Section 3.2).

We apply standard InSAR processing using the JPL/Caltech ROI_PAC software (Rosen *et al.* 2004), and construct 52 interferograms (listed in Table 2). Most of the interferograms span longer than one year, helping to better detect long-term crustal deformation signals and to avoid inadvertently including contributions from ice motion occurring at the glacier–bedrock boundary. Lateral ice displacements over one year or longer are typically more than several kilometres, and thus show no coherence in our interferograms. We take 32 looks in both the range and azimuth directions, corresponding to ground pixel resolutions of ∼250 m and ∼180 m, respectively. Multi-looked interferograms exhibit enhanced coherence and still keep the deformation signals of interest at a relatively high spatial resolution.

To measure ground surface deformation, we remove the topographic contributions to the InSAR-measured radar phase changes using the known orbital positions (we refer to this step as 'topography removal'). We construct a digital elevation model (DEM) using the Advanced Spaceborne Thermal Emissivity and Reflection Radiometer (ASTER) imagery (see Howat *et al.* 2008, for a detailed description). In all interferograms, we mask out DEM artefacts that occur over large water bodies and some cloud-covered areas. For topography removal, we use the raw orbit products distributed by CSA. We correct for orbit errors using the technique described in the following section. Finally, we stack the geocoded and unwrapped interferograms using the method described by Biggs *et al.* (2007) to estimate the deformation rate and to reduce artefacts due to atmospheric delay and residual orbit errors that are not fully removed.

3.2 Correcting InSAR orbit errors using conventional methods

The InSAR baseline, the geometric separation of the radar antenna at two SAR acquisitions, is required for topography removal. The baseline and its temporal variation are usually calculated with *a priori* information such as the orbit ephemeris provided by the

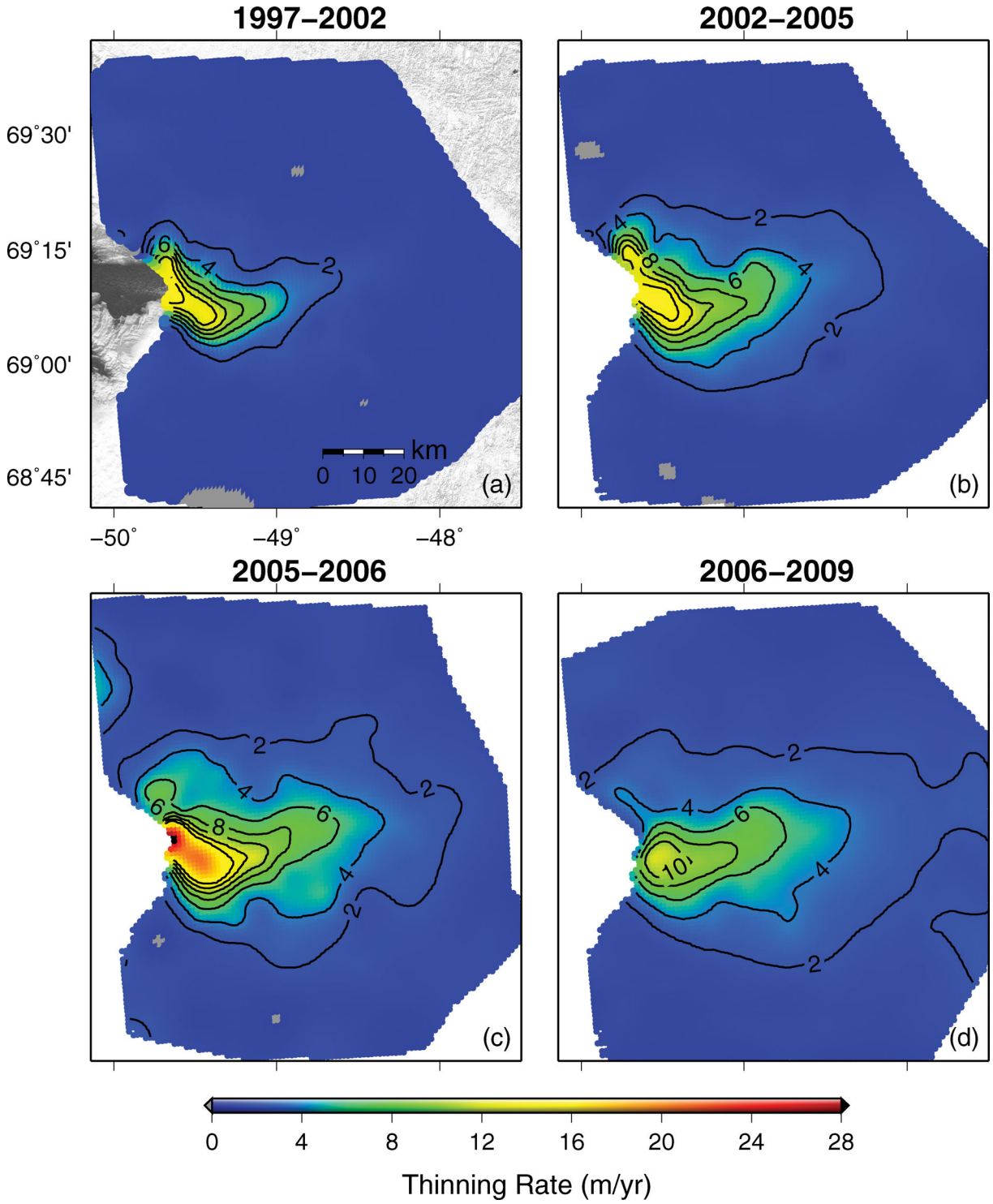

Figure 2. Maps of glacial thinning rates at Jakobshavn Isbræ based on ATM repeat laser-altimetry surveys: (a) between 1997 and 2002, (b) between 2002 and 2005, (c) between 2005 and 2006 (only contours up to 14 m yr^{-1} are shown) and (d) between 2006 and 2009. Figs (a)–(c) and (d) are reproduced from Joughin *et al.* (2008) and Khan *et al.* (2010a), respectively, using data distributed by NASA Wallops (Krabill 2009). Positive values indicate thinning. Grey represents slight thickening with rates smaller than 0.5 m yr^{-1}.

satellite control agencies and post-processed precise orbit products. Because Radarsat-1 was not designed for InSAR applications, its orbit position was determined to a relatively low accuracy, on the order of 10 m (Parashar & Langham 1997).

InSAR orbit errors (errors in LOS range changes caused by baseline errors) resemble a long-wavelength pattern in an unwrapped interferogram, and nearly parallel fringes in a wrapped interferogram. Fig. 4(a) shows a typical Radarsat-1 interferogram dominated by orbit error fringes, which vary across the image by about 18 cm.

We use a baseline fitting approach implemented in ROI_PAC (Rosen *et al.* 1996; Buckley *et al.* 2000). This method estimates five baseline parameters: baseline offsets in the vertical and

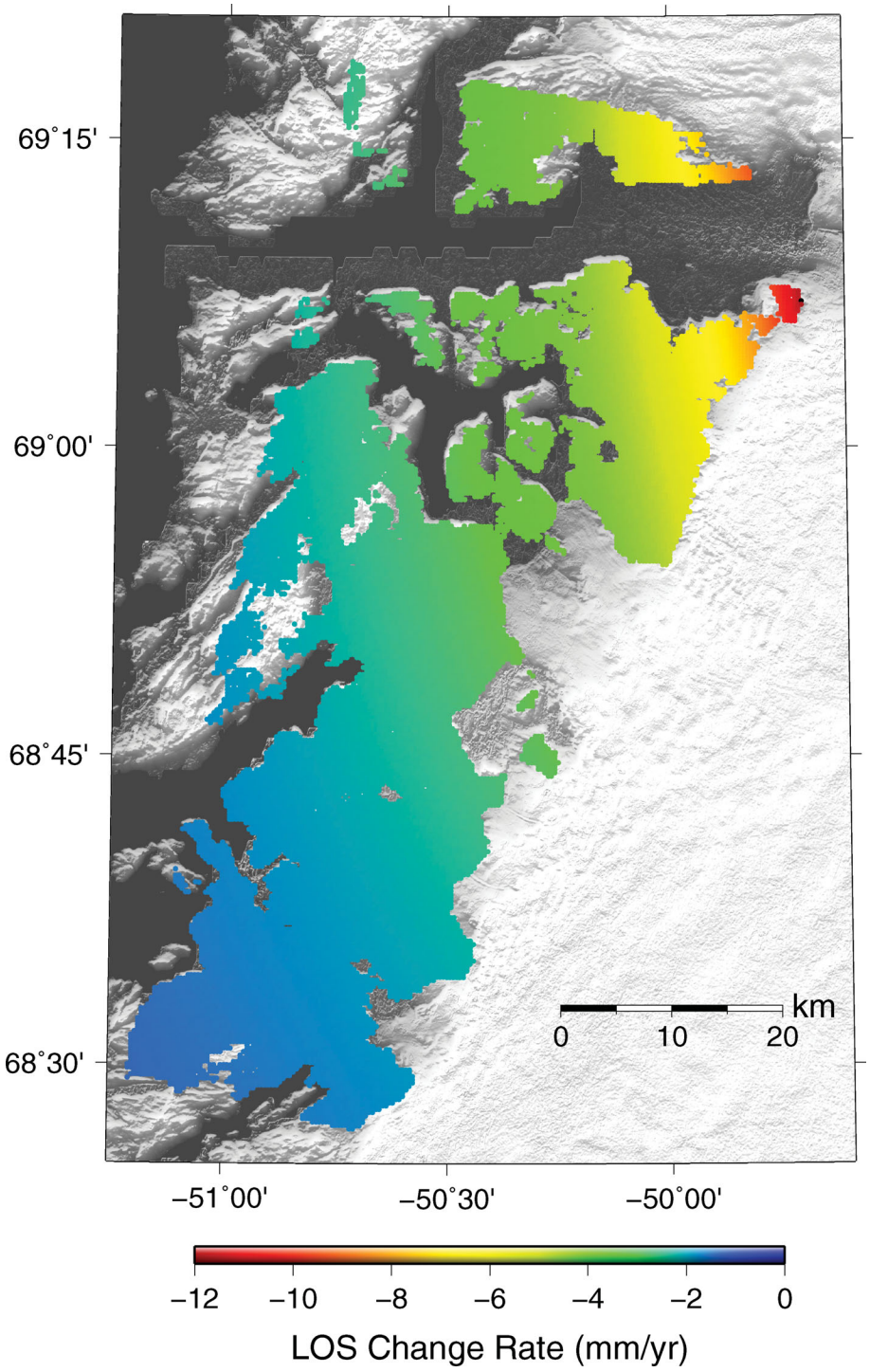

Figure 3. Map of the predicted Radarsat-1 LOS rates at InSAR gridpoints between 2004 September and 2008 April. The background image is the same as in Fig. 1. Negative values mean shortening in LOS distance, largely due to crustal uplift.

horizontal directions, rates of baseline change with respect to the along-track position in the master-scene trajectory in both directions, and a constant phase offset. Baseline errors in the along-track direction are corrected during coregistration of the two SAR images (Hanssen 2001). We prefer to fit baseline parameters rather than to fit a specific spatial pattern because the former better represents the baseline geometry and requires no empirical assumptions of orbit error patterns.

The InSAR-observed change in the LOS range r_i at a point located at x_i consists of a deformation signal d_i, a contribution from surface topography f_i, and errors ε_i, that is,

$$r_i = d_i + f_i + \varepsilon_i. \tag{2}$$

We represent f_i with a geometric function $\tilde{f}(x_i; \boldsymbol{a})$ that depends non-linearly on the five baseline parameters $(a_1, a_2, \ldots, a_5) = \boldsymbol{a}$, and that has a long-wavelength spatial dependence across a

Table 1. Radarsat-1 SAR scenes (in descending orbits) used in this study. Dates of SAR acquisitions are in the format 'yyyymmdd'.

Date	Orbit number	Date	Orbit number
20040921	46360	20060701	55621
20041015	46703	20060818	56307
20041226	47732	20060911	56650
20050119	48075	20061005	56993
20050212	48418	20061122	57679
20050308	48761	20070109	58365
20050401	49104	20070226	59051
20050519	49790	20070322	59394
20050730	50819	20070509	60080
20050823	51162	20070626	60766
20050916	51505	20070720	61109
20051010	51848	20070813	61452
20051127	52534	20070906	61795
20060114	53220	20070930	62138
20060207	53563	20080104	63510
20060303	53906	20080221	64196
20060327	54249	20080316	64539
20060514	54935	20080409	64882

scene. See the detailed expression of $\tilde{f}(x_i; \boldsymbol{a})$ in Buckley *et al.* (2000).

Given N observations $(r_1, r_2, \ldots, r_N)$ in one interferogram, the goal of baseline fitting is to solve for $\boldsymbol{a}$, which minimizes the difference between the observed range change and the range change due to surface topography only. The merit function we minimize is

$$E = \frac{1}{N} \sum_{i=1}^{N} \left[\frac{r_i - \tilde{f}_i(\boldsymbol{a})}{\sigma_i} \right]^2, \tag{3}$$

where σ_i is the measurement error. Here we assume the errors at individual pixels are identical and independent of each other. Combining (2) and (3), we note that by minimizing E we absorb the long-wavelength components of $\mathbf{d}$ (and of ε) into our solution for $\tilde{\boldsymbol{f}}(\boldsymbol{a})$.

Fig. 4(b) shows the residual Radarsat-1 interferogram after fitting and removing orbit errors using pixels evenly distributed across the entire scene (hereafter referred to as 'full-scene baseline fitting'). Short-wavelength (less than 5 km) features become visible, including some LOS shortening signals on the northeast tips near the glacier front, as well as atmospheric artefacts (e.g. the wavy features near the centre). The LOS shortening signals in the northeast are common to most of the other residual interferograms, indicating that they are probably real deformation signals. We apply the same full-scene baseline fitting to the ATM-based synthetic interferogram shown in Fig. 4(d), and obtain the residual synthetic map shown in Fig. 4(e). As expected, the baseline fitting process removes long-wavelength signals, but still leaves LOS shortening signals on the northeast tips.

To retain more of the long-wavelength deformation signals across the region near the glacier, we repeat the baseline fitting process, but fit only to the area south of Tiningnilik Lake (south of the dashed line in Fig. 4c). This area is in the far field of the deformation, where the InSAR observations are dominated by orbit errors. We use these fitted baseline parameters to correct the orbit errors in the north, under the assumption that there is little variation in the baseline

Table 2. Interferograms constructed and used in this study. Names of interferograms are in the format 'yyyymmdd-yyyymmdd'. The dates before and after the hyphen are the master and slave scenes, respectively. Column 'B perp' lists the perpendicular satellite baselines in metres between the two SAR scenes. Column 'Time interval' lists the time span of each interferogram in days.

Interferogram	B perp	Time interval	Interferogram	B perp	Time interval
20040921-20050916	66.8	359	20050401-20070930	−11.0	911
20040921-20060911	92.2	719	20050519-20070226	71.8	648
20040921-20070720	−16.8	1032	20050519-20070322	74.5	672
20040921-20080104	57.9	1200	20050730-20070626	17.9	696
20040921-20080221	74.1	1248	20050823-20070226	−42.8	552
20041015-20051127	99.4	408	20050823-20070322	−40.1	575
20041015-20060207	57.4	480	20050916-20060911	25.4	359
20041015-20070720	−125.8	1007	20050916-20070720	−83.5	672
20041015-20070813	−23.2	1032	20050916-20080104	−8.9	840
20041015-20080104	−51.1	1176	20050916-20080221	7.3	888
20041226-20061122	−81.8	696	20051010-20070226	−61.4	504
20041226-20070109	−79.8	744	20051010-20070322	−58.7	528
20050119-20060207	−1.4	383	20051127-20061122	63.2	359
20050119-20060514	−20.1	479	20051127-20070109	65.2	408
20050119-20060701	−46.7	527	20060114-20070109	67.9	359
20050119-20061122	103.8	672	20060207-20070109	107.2	336
20050212-20061122	19.3	647	20060207-20070813	−80.6	551
20050212-20070109	21.3	696	20060207-20080221	−92.3	744
20050212-20070509	2.6	815	20060303-20080316	52.7	743
20050308-20070226	5.2	719	20060327-20070813	−91.3	503
20050308-20070322	7.9	743	20060514-20070509	107.2	359
20050308-20070906	3.4	911	20060701-20070813	−35.3	408
20050308-20070930	−100.7	935	20060818-20080316	35.9	575
20050401-20061005	2.1	551	20060911-20070813	−6.4	336
20050401-20070226	94.9	696	20060911-20080221	−18.1	528
20050401-20070322	97.5	719	20070322-20080409	15.2	383

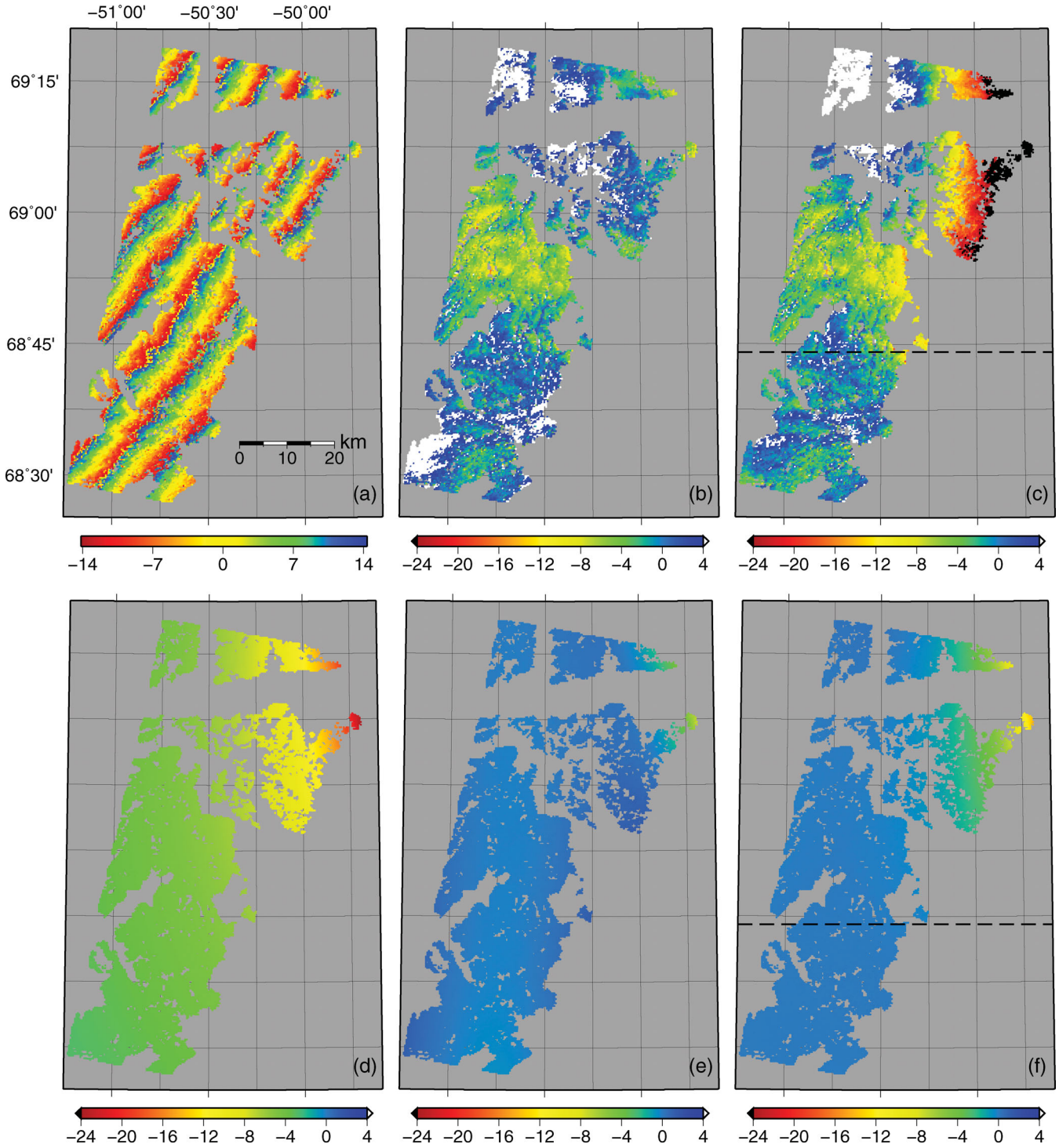

Figure 4. Examples of the interferogram 20050730-20070626 (in millimetres): (a) wrapped interferogram dominated by orbital fringes, (b) residual interferogram after applying full-scene baseline fitting, (c) residual interferogram after applying far-field (defined as the area south of the dashed line) baseline fitting, (d) synthetic interferogram produced by multiplying the ATM-derived deformation rates by the interferogram time span, (e) residual synthetic interferogram after applying full-scene baseline fitting and (f) residual synthetic interferogram after applying far-field baseline fitting.

parameters over 100 km—the approximate distance from south to north in the interferogram. As shown in the residual interferogram (Fig. 4c), only short-scale signals are left in the southern area. In the north, a large gradient of about 1 mm km^{-1} still remains in the east–west direction, which is consistent with that of the predicted deformation (Fig. 4d), but with a larger magnitude. Fig. 4(f) shows the residual synthetic interferogram. The differences between Figs 4(d) and (f) are caused by the existing long-wavelength deformation signals in the far field, which bias the baseline fitting and introduce errors into the solution in the north.

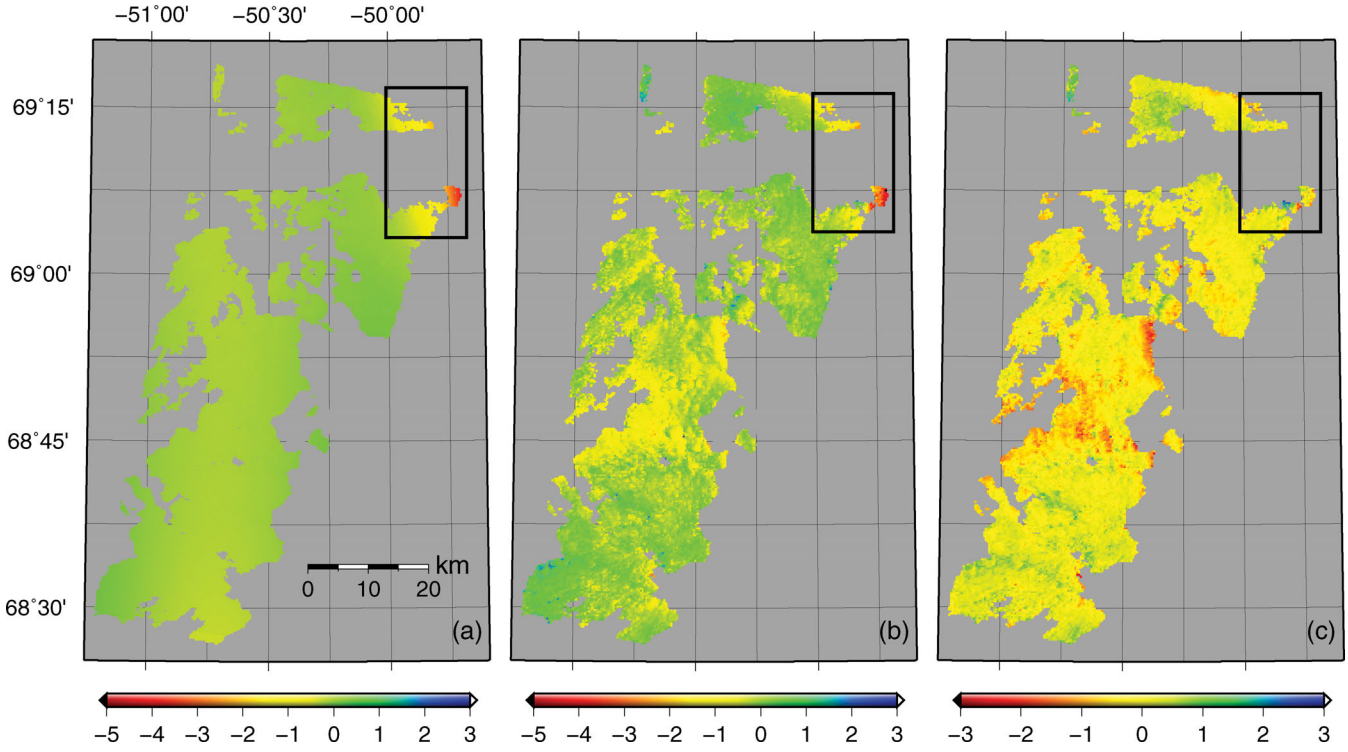

Figure 5. Maps of stacked LOS rates (in mm yr^{-1}) after applying the full-scene baseline fitting: (a) from the predictions based on the ATM surveys; (b) from the Radarsat-1 interferograms and (c) the differences (InSAR minus predictions). Negative rates in (a) and (b) indicate LOS shortening. The areas in grey are those where no robust InSAR measurements can be made. The black box in each plot outlines the region close to the glacier, where we find good agreement between the InSAR and prediction results.

3.3 InSAR stacking results

In this section, we examine the linear deformation rates obtained using the full-scene and the far-field baseline fitting methods. Figs 5(a) and (b) show maps of the deformation rates in the LOS direction, calculated by stacking the synthetic and Radarsat-1 interferograms, respectively, after applying the full-scene baseline fitting. Compared with the deformation model shown in Fig. 3, the predicted rates (Fig. 5a) contain only short-scale components. The area near the glacier (outlined by the black box in Fig. 5a) shows the largest LOS shortening rates of up to 5 mm yr^{-1}. At distances of about 15 km and further away, the LOS rates drop to around zero. Fig. 5(c) plots the differences between the two sets of rates, showing generally good agreement within 1 mm yr^{-1}. The differences in the central area are likely caused by atmospheric delay errors.

Similarly, Figs 6(a) and (b) show the maps of the stacked LOS rates, based on the synthetic and Radarsat-1 interferograms, respectively, but using the far-field baseline fitting. The area near the glacier shows the largest LOS shortening rates of up to about 8 mm yr^{-1}, which drop to around zero at distances of about 20 km and further away. As is evident by comparing Fig. 6(a) with Fig. 5(a), we are able to recover more of the long-wavelength deformation with the far-field fitting. However, the recovered signals are still different than those in the original deformation model (Fig. 3), due to the fact that a long-wavelength deformation signal exists in the far field. The inversion results based on the Radarsat-1 interferograms (Fig. 6b) show similar features near the glacier. Again, we find good agreement between the InSAR results and the predictions.

In summary, although conventional baseline fitting methods remove much of the long-wavelength unloading deformation from interferograms, we are still able to measure significant short-wavelength components of the unloading deformation, especially near the glacier front. The good agreement between the InSAR-measured and the predicted LOS rates confirms the accuracy of the ATM data and the appropriateness of using a constant ice density to convert the AMT-measured elevation changes to ice mass changes.

4 INVERTING FOR ICE UNLOADING

In addition to validating the ATM surveys, we have used the InSAR-measured crustal displacements to directly invert for the pattern and magnitude of ice mass loss on Jakobshavn Isbræ. Each of our high-resolution maps (Figs 5b and 6b) of the LOS rate contains over 10 000 pixels, making it possible to invert for the ice mass loss over the glacier drainage basin. Moreover, an inversion solution can be used to determine the regions of the glacier that have the greatest impact on the short-wavelength InSAR deformation field. It can thus be used to better understand the implications of the InSAR/ATM comparison described in Section 3.

The inversion problem, however, is ill-posed because the load process is non-unique (i.e. a large load at long distances and a small loading at short distances could cause the same amount of deformation at an InSAR pixel). The fact that the deformation field lies off to only one side of the drainage basin increases the difficulty. To stabilize the inversion, we use second-order Tikhonov regularization (Aster *et al.* 2005) by adaptively placing smoothing constraints on the fitted thinning rates (see the Appendix for the detailed inversion algorithm).

We test this inversion algorithm using a synthetic data set. We use the 2005–2006 ATM unloading (resampled at 5 km resolution,

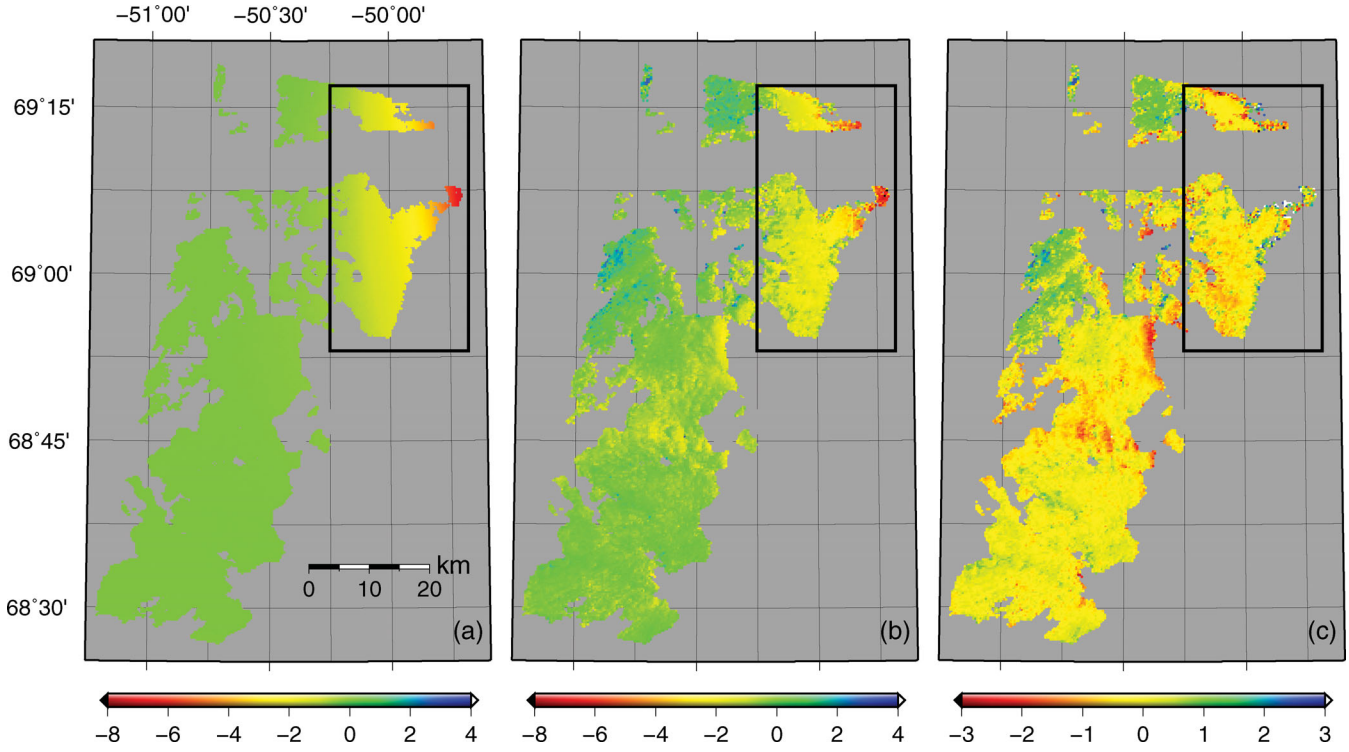

Figure 6. Similar to Fig. 5. Maps of LOS rates (in mm yr^{-1}) after applying the far-field baseline fitting: (a) from the predictions based on the ATM surveys; (b) from the Radarsat-1 interferograms and (c) InSAR minus predictions.

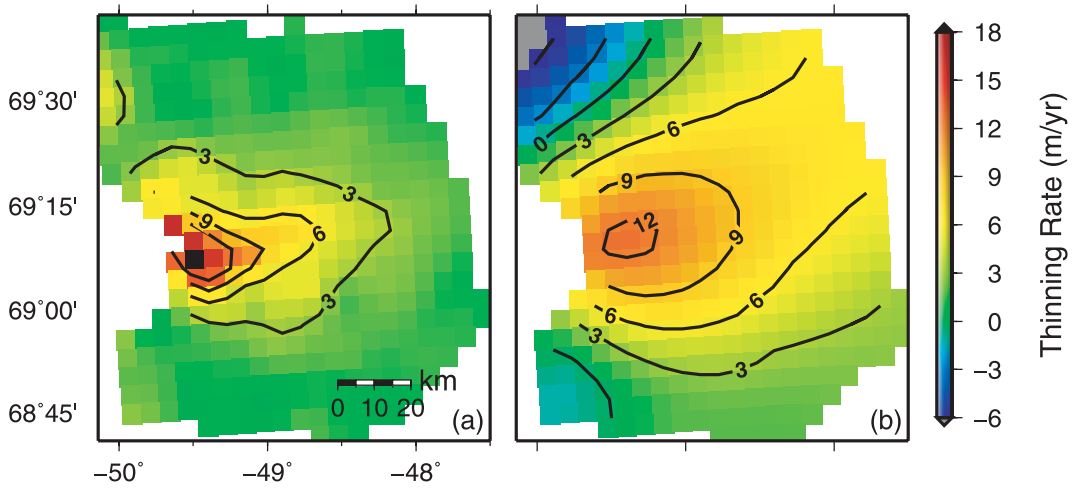

Figure 7. Ice thinning maps: (a) synthetic thinning model based on the ATM surveys in 2005 and 2006 (resampled from Fig. 2c), (b) inverted thinning using the synthetic deformation field produced using (a).

and shown in Fig. 7a) to calculate LOS deformation, which is then inverted to obtain the ice thinning rates shown in Fig. 7(b). Comparing Figs 7(a) and (b) shows that the inversion solution recovers the general spatial pattern of ice unloading concentrated in the trunk of the glacier, but that it loses short-scale features in the north–south direction and smears the unloading towards the east. In addition, it causes an artificial positive loading signal in the northwest corner. For this reason, we ignore any signal that shows up in this corner when interpreting inversions that use real InSAR data.

We obtain four ice unloading models by inverting the following deformation fields north of 68.85°N (where the deformation signals are strongest), as described in Sections 2 and 3.3: (1) synthetic and (2) InSAR LOS rates, after applying full-scene fitting (as shown in Figs 5a and b, respectively), (3) synthetic and (4) InSAR LOS rates after applying far-field baseline fitting (as shown in Figs 6a and b, respectively). The inversion results are shown in Figs 8(a)–(d), respectively. All these maps show significant thinning near the grounding line along the glacier trunk, and gradually decreasing thinning inland towards the east.

We compare these results from two perspectives. First, we find consistent patterns between the inversion results based on the synthetic data (Figs 8a and c) and the corresponding inversion results based on the InSAR measurements (Figs 8b and d). This reinforces our Section 3.3 conclusion that the ATM-derived and

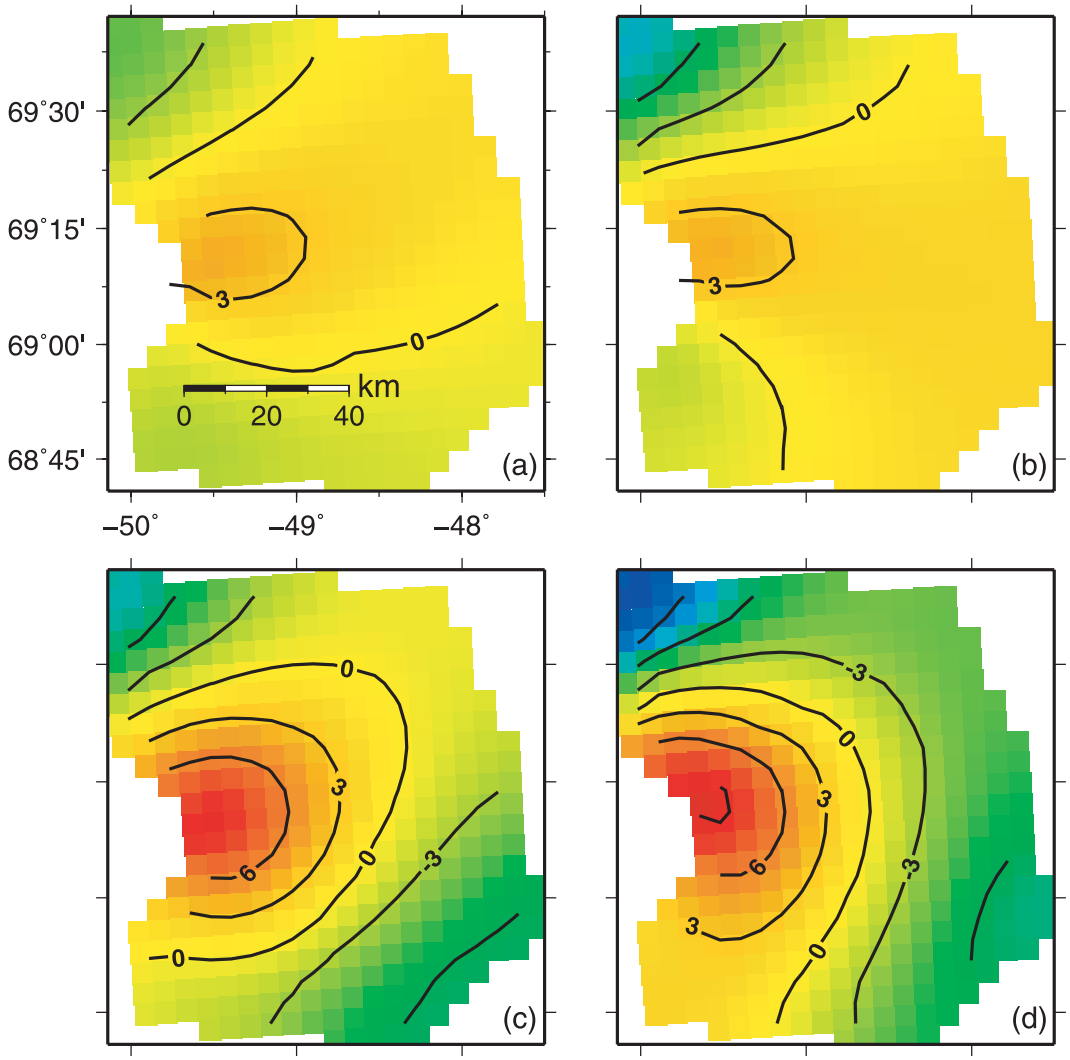

Figure 8. Ice thinning maps inverted from (a) stacked LOS rates after applying full-scene baseline fitting to synthetic interferograms; (b) stacked LOS rates after applying full-scene baseline fitting to Radarsat-1 interferograms; (c) stacked LOS rates after applying far-field baseline fitting to synthetic interferograms; (d) stacked LOS rates after applying far-field baseline fitting to Radarsat-1 interferograms.

InSAR-measured deformation rates are consistent at both short and long wavelengths. Secondly, the spatial patterns of the inversion results provide insight on what areas of unloading the InSAR-measured deformation is sensitive to. Figs 8(a) and (b) show unloading localized within ∼20 km of the grounding line. This implies that the full-scene baseline fitting results derived in Section 3 are mostly sensitive to the ice unloading within this localized area. When applying the far-field baseline fitting, we observe a larger unloading area (Figs 8c and d), 40–50 km away from the grounding line.

5 DISCUSSION AND CONCLUSIONS

5.1 Unmodelled error sources

We do not model artefacts in the interferograms caused by atmospheric delay (Zebker *et al.* 1997), ionospheric signals (Gray *et al.* 2000), or changes in snow cover. An interferogram made from differencing a snow-covered SAR scene and a snow-free scene could show an apparent LOS-lengthening signature, as radar waves are delayed when propagating through snow. Furthermore, the surface permittivity varies significantly for dry snow, wet snow, cold firn or ice (Hoen & Zebker 2000; König *et al.* 2001; Rignot *et al.* 2001), resulting in artificial LOS changes. Similar to the differential atmospheric and ionospheric signals, artefacts due to changes in surface snow cover would be distributed randomly in time, as our interferograms are made from pairs of winter minus summer, summer in previous years minus winter, late winter minus early winter and early winter minus late winter in previous years. Therefore, when we stack 52 interferograms to obtain deformation rates over about four years, those temporally random effects tend to be filtered out. In addition, none of these errors are likely to cause linear LOS shortening rates concentrated locally in the northeast area near the glacier.

The long-wavelength components of these unmodelled errors in individual interferograms, together with the long-wavelength errors in the PGR and OTL models, could potentially be indistinguishable from InSAR orbit errors. This is not a serious problem when we apply full-scene baseline fitting, as we remove most of the

long-wavelength signals anyway; or when we stack the interferograms after applying the far-field baseline fitting, since the long-wavelength errors still appear to vary randomly with time.

5.2 Strengths and weaknesses of InSAR deformation measurements for studying ice mass balance

The greatest strength of InSAR deformation measurements for ice mass balance studies is their extensive spatial coverage and high spatial resolution. In effect, InSAR provides a large number of ground measurements that can be used to constrain existing ice mass balance models and to directly invert for ice mass changes. In addition, InSAR-measured deformation places direct constraints on ice mass changes within a drainage basin, without requiring knowledge of the surface density profile.

However, the orbital positions of satellites flying over polar areas are usually not well determined due to sparse ground tracking stations, resulting in large InSAR orbit errors. As demonstrated in Section 3.3, conventional full-scene baseline fitting removes most of the long-wavelength deformation signals, but is still able to provide constraints on short-scale loading. Far-field baseline fitting keeps much of the long-wavelength signal, although real deformation signals over the defined far-field could bias the baseline fitting results.

For the first time, we are able to directly invert for ice mass changes from InSAR measurements. This inversion requires no *a priori* information on glacial ice mass balance, except for general knowledge of the spatial extent where the ice mass is changing to reduce the degree of non-uniqueness. Therefore, this method can be used to provide information on ice mass loss for a drainage basin in the absence of any measurements from the glacier itself. However, due to InSAR orbit errors, inversions based solely on InSAR observations can only provide information on the general spatial pattern. Ground-based deformation measurements, which could be used together with InSAR measurements in the inversion, would be useful to help resolve this problem.

5.3 Concluding remarks

In this paper, we apply InSAR to Radarsat-1 SAR data to determine crustal deformation near Jakobshavn Isbræ. Using full-scene and far-field baseline fitting, we find significant LOS shortening over the bedrock area near the glacier, with rates of up to 5 mm yr^{-1} and 8 mm yr^{-1} during 2004–2008, respectively. We find good agreement between the InSAR observations and predictions based on repeat ATM surveys of Jakobshavn Isbræ elevations. This agreement reinforces our confidence in the quality of the ice mass loss estimates derived from the ATM surveys. In addition, we are able to directly invert for ice thinning from the InSAR-measured deformation. Our inversion illustrates a different and more direct method of using InSAR observations to validate ice thinning at various spatial scales.

InSAR orbit errors pose by far the greatest challenge for constructing the full deformation field caused by glacial unloading. It is possible to alleviate this problem by using GPS measurements as ground control points during baseline fitting, provided enough GPS sites are within InSAR frames (Liu 2011).

These new applications of InSAR can be applied to other areas where significant ice mass loss is occurring. They can potentially improve estimates of glacial ice mass balance, and can thus increase our understanding of the dynamic behaviour of the polar ice sheets, which is still the source of considerable uncertainty in predictions of future sea level change.

ACKNOWLEDGMENTS

We thank Eric Fielding and Paul Lundgren for their help on ROI_PAC. We thank Matt Pritchard for providing programs to process Radarsat-1 data (Pritchard *et al.* 2007). We also thank two anonymous reviewers and Isabella Velicogna for their helpful comments. We thank the NASA Wallops Flight Facility and the National Snow and Ice Data Center for providing the ATM data. The Radarsat-1 SAR data are copyrighted by the CSA and provided by the Alaska Satellite Facility. This work was partially supported by NASA Grants NNX06AH37G and NNX06AE65G to the University of Colorado, and by NASA Headquarters under the Earth and Space Science Fellowship Program—NNX08AU85H.

REFERENCES

Agnew, D., 1997. NLOADF: a program for computing ocean-tide loading, *J. geophys. Res.,* **102**(B3), 5109–5110.

Aster, R., Thurber, C. & Borchers, B., 2005. *Parameter Estimation and Inverse Problems,* Academic Press, Amsterdam.

Bevis, M. *et al.*, 2009. Geodetic measurements of vertical crustal velocity in West Antarctica and the implications for ice mass balance, *Geochem. Geophys. Geosyst.,* **10**(10), Q10005, doi:10.1029/2009GC002642.

Biggs, J., Wright, T., Lu, Z. & Parsons, B., 2007. Multi-interferogram method for measuring interseismic deformation: Denali fault, Alaska, *Geophys. J. Int.,* **170**(3), 1165–1179.

Buckley, S., Rosen, P. & Persaud, P., 2000. Radar interferometry measurement of land subsidence, *PhD thesis,* University of Texas at Austin, ch. 3.

Cuffey, K. & Paterson, W., 2010. *The Physics of Glaciers,* Oxford, Butterworth-Heinemann.

DiCaprio, C. & Simons, M., 2008. Importance of ocean tidal load corrections for differential InSAR, *Geophys. Res. Lett.,* **35**(22), L22309, doi:10.1029/2008GL035806.

Dietrich, R., Rülke, A. & Scheinert, M., 2005. Present-day vertical crustal deformations in West Greenland from repeated GPS observations, *Geophys. J. Int.,* **163**(3), 865–874.

Dietrich, R., Ivins, E., Casassa, G., Lange, H., Wendt, J. & Fritsche, M., 2010. Rapid crustal uplift in Patagonia due to enhanced ice loss, *Earth planet. Sci. Lett.,* **289**(1–2), 22–29.

Farrell, W.E., 1972. Deformation of Earth by surface loads, *Rev. Geophys. Space Phys.,* **10**(3), 761–797, doi:10.1029/RG010i003p00761.

Furuya, M. & Wahr, J., 2005. Water level changes at an ice-dammed lake in west Greenland inferred from InSAR data, *Geophys. Res. Lett.,* **32**(14), L14501, doi:10.1029/2005GL023458.

Goldstein, R., Engelhardt, H., Kamb, B. & Frolich, R., 1993. Satellite radar interferometry for monitoring ice sheet motion: application to an Antarctic ice stream, *Science,* **262**(5139), 1525–1530.

Gray, A., Mattar, K. & Sofko, G., 2000. Influence of ionospheric electron density fluctuations on satellite radar interferometry, *Geophys. Res. Lett.,* **27**(10), 1451–1454.

Hanssen, R.F., 2001. *Radar Interferometry: Data Interpretation and Error Analysis,* Kluwer Academic Publishers, Dordrecht.

Hoen, W. & Zebker, H., 2000. Penetration depths inferred from interferometric volume decorrelation observed over the Greenland Ice Sheet, *IEEE Trans. Geosci. Remote Sens.,* **38**(6), 2571–2583.

Howat, I., Smith, B., Joughin, I. & Scambos, T., 2008. Rates of southeast Greenland ice volume loss from combined ICESat and ASTER observations, *Geophys. Res. Lett.,* **35**(17), L17505, doi:10.1029/2008GL034496.

Joughin, I., 2002. Ice-sheet velocity mapping: a combined interferometric and speckle-tracking approach, *Ann. Glaciol.,* **34**(1), 195–201.

Joughin, I., Kwok, R. & Fahnestock, M., 1996. Estimation of ice-sheet motion using satellite radar interferometry: method and error analysis with application to Humboldt Glacier, Greenland, *J. Glaciol.,* **42**(142), 564–575.

Joughin, I., Abdalati, W. & Fahnestock, M., 2004. Large fluctuations in speed on Greenland's Jakobshavn Isbræ glacier, *Nature,* **432**(7017), 608–610.

Joughin, I., Howat, I., Fahnestock, M., Smith, B., Krabill, W., Alley, R., Stern, H. & Truffer, M., 2008. Continued evolution of Jakobshavn Isbrae following its rapid speedup, *J. geophys. Res.,* **113**(F4), F04006, doi:10.1029/2008JF001023.

Khan, S., Wahr, J., Stearns, L., Hamilton, G., van Dam, T., Larson, K. & Francis, O., 2007. Elastic uplift in southeast Greenland due to rapid ice mass loss, *Geophys. Res. Lett.,* **34**(21), L21701, doi:10.1029/2007GL031468.

Khan, S.A., Liu, L., Wahr, J., Howat, I., Joughin, I., van Dam, T. & Fleming, K., 2010a. GPS measurements of crustal uplift near Jakobshavn Isbræ to glacial ice mass loss, *J. geophys. Res.,* **115**(B9), B09405, doi:10.1029/2010JB007490.

Khan, S.A., Wahr, J., Bevis, M., Velicogna, I. & Kendrick, E., 2010b. Spread of ice mass loss into northwest Greenland observed by GRACE and GPS, *Geophys. Res. Lett.,* **37**(6), L06501, doi:10.1029/2010GL042460.

Kierulf, H., Plag, H. & Kohler, J., 2009. Surface deformation induced by present-day ice melting in Svalbard, *Geophys. J. Int.,* **179**(1), 1–13.

König, M., Winther, J. & Isaksson, E., 2001. Measuring snow and glacier ice properties from satellite, *Rev. Geophys.,* **39**(1), 1–27.

Krabill, W., 2009. *IceBridge ATM L2 Icessn Elevation, Slope, and Roughness (March to June 2009)*, National Snow and Ice Data Center, Boulder, CO (http://nsidc.org/data/ilatm2.html).

Krabill, W. *et al.*, 1999. Rapid thinning of parts of the southern Greenland ice sheet, *Science,* **283**(5407), 1522–1524.

Krabill, W. *et al.*, 2000. Greenland ice sheet: high-elevation balance and peripheral thinning, *Science,* **289**(5478), 428–430.

Krabill, W. *et al.*, 2004. Greenland ice sheet: increased coastal thinning, *Geophys. Res. Lett.,* **31**(24), L24402, doi:10.1029/2004GL021533.

Liu, L., 2011. Studying changes in the cryosphere using radar interferometry: permafrost surface subsidence and glacial unloading deformation, *PhD thesis*, University of Colorado.

Parashar, S. & Langham, E., 1997. Operational qualification of RADARSAT, *Adv. Space Res.,* **19**(9), 1437–1445.

Peltier, W.R., 2004. Global glacial isostasy and the surface of the ice-age Earth: the ICE-5G (VM2) model and GRACE, *Annu. Rev. Earth planet. Sci.,* **32**, 111–149.

Pritchard, M.E., Norabuena, E.O., Ji, C., Boroschek, R., Comte, D., Simons, M., Dixon, T.H. & Rosen, P.A., 2007. Geodetic, teleseismic, and strong motion constraints on slip from recent southern peru subduction zone earthquakes, *J. geophys. Res.,* **112**(B3), B03307, doi:10.1029/2006JB004294.

Ray, R., 1999. A Global Ocean Tide Model from TOPEX/POSEIDON Altimetry: GOT99. 2, *NASA Technical Memo. 209478,* Goddard Space Flight Center, Greenbelt, MD, 58pp.

Rignot, E. & Kanagaratnam, P., 2006. Changes in the velocity structure of the Greenland Ice Sheet, *Science,* **311**(5763), 986–990.

Rignot, E., Gogineni, S., Krabill, W. & Ekholm, S., 1997. North and northeast Greenland ice discharge from satellite radar interferometry, *Science,* **276**(5314), 934–937.

Rignot, E., Echelmeyer, K. & Krabill, W., 2001. Penetration depth of interferometric synthetic-aperture radar signals in snow and ice, *Geophys. Res. Lett.,* **28**(18), 3501–3504.

Rosen, P., Hensley, S., Zebker, H., Webb, F. & Fielding, E., 1996. Surface deformation and coherence measurements of Kilauea Volcano, Hawaii, from SIR-C radar interferometry, *J. geophys. Res.,* **101**(E10), 23 109–23 125.

Rosen, P.A., Henley, S., Peltzer, G. & Simons, M., 2004. Update repeat orbit interferometry package released, *EOS, Trans. Am. geophys. Un.,* **85**, 47–47.

Sauber, J. & Molnia, B., 2004. Glacier ice mass fluctuations and fault instability in tectonically active southern Alaska, *Glob. planet. Change,* **42**(1–4), 279–293.

Shewchuk, J., Lin, M. & Manocha, D., 1996. Triangle: Engineering a 2D quality mesh generator and Delaunay triangulator, *Applied Computational Geometry Towards Geometric Engineering,* Lecture Notes in Computing Science vol. 1148, eds Lin, M.C. & Manocha D., pp. 203–222, Springer, Berlin, doi: 10.1007/BFb0014497.

Thomas, R., Abdalati, W., Frederick, E., Krabill, W., Manizade, S. & Steffen, K., 2003. Investigation of surface melting and dynamic thinning on Jakobshavn Isbræ, Greenland, *J. Glaciol.,* **49**(165), 231–239.

Thomas, R., Frederick, E., Krabill, W., Manizade, S. & Martin, C., 2009. Recent changes on Greenland outlet glaciers, *J. Glaciol.,* **55**(189), 147–162.

Zebker, H.A., Rosen, P.A. & Hensley, S., 1997. Atmospheric effects in interferometric synthetic aperture radar surface deformation and topographic maps, *J. geophys. Res..,* **102**(B4), 7547–7563.

APPENDIX A: ICE UNLOADING INVERSION AND ADAPTIVE SMOOTHING

This appendix describes the inversion algorithm used to invert for ice unloading from the InSAR-measured crustal deformation. In matrix form, eq. (1) can be rewritten as

$$\mathbf{d} = \mathbf{G}\mathbf{u}, \tag{A1}$$

where **d** and **u** are the deformation vector and the ice thinning vector, respectively; and **G** is the elastic loading operator in the LOS direction. This forward problem is a linear convolution of the loading with the elastic-loading Green's function.

Given a set of deformation data (d_1, d_2, ..., d_M), the inverse problem is to solve for the ice thinning rates (u_1, u_2, ..., u_N) that minimize

$$S = \sum_{i=1}^{M} \left[d_i - \sum_{j=1}^{N} g_{i,j} u_j \right]^2, \tag{A2}$$

where we have assumed the same measurement uncertainty at all deformation pixels. However, in practice **G** is likely to be nearly singular, causing the inversion to be ill-posed.

To stabilize the inversion, we minimize a new merit function, extending (A2), to be

$$S' = \sum_{i=1}^{M} \left[d_i - \sum_{j=1}^{N} g_{i,j} u_j \right]^2 + \lambda \sum_{j=1}^{N} \left[u_j - \frac{1}{4} \sum_{k=1}^{4} u_j^k \right]^2, \tag{A3}$$

where the second term on the right-hand side describes the spatial gradient between a loading point u_j and its four nearest neighbours (u_j^1, u_j^2, u_j^3, and u_j^4). The parameter λ, chosen to have a non-negative value, defines the strength of the smoothing.

We define a 'roughness matrix' **B** to represent the spatial gradient term in eq. (A3). In the *i*th row of **B**, corresponding to the *i*th loading point, the *i*th column is 1; the values in the four columns corresponding to its four nearest neighbours are $-1/4$; and all the other column values are zero. Then, we rewrite eq. (A3) in matrix form as

$$S' = |\mathbf{d} - \mathbf{G}\mathbf{u}|^2 + \lambda |\mathbf{B}\mathbf{u}|^2, \tag{A4}$$

in which $|\cdot|$ denotes the vector length. The value of **u** that minimizes eq. (A4) is

$$\mathbf{u} = (\mathbf{G}^{\mathrm{T}}\mathbf{G} + \lambda \mathbf{B}^{\mathrm{T}}\mathbf{B})^{-1}\mathbf{G}^{\mathrm{T}}\mathbf{d}, \tag{A5}$$

in which $(\cdot)^{\mathrm{T}}$ and $(\cdot)^{-1}$ denote the matrix transpose and inverse, respectively.

In practice, to reduce the computation load we undersample the deformation field by using only measurements north of 68.85°N where the deformation signals are strongest. We represent the ice unloading field with a grid that covers the same area as the ATM ice mass unloading map, with a grid spacing of 5 km. On this 2-D ice

grid, we use 'Triangle', a Delaunay Triangulator (Shewchuk 1996), to find the nearest neighbour points and to construct the matrix **B**.

The resolution matrix in model space is defined as

$$\mathbf{R} = (\mathbf{G}^{\mathrm{T}}\mathbf{G} + \lambda\mathbf{B}^{\mathrm{T}}\mathbf{B})^{-1}\mathbf{G}^{\mathrm{T}}\mathbf{G}. \tag{A6}$$

It describes how the solution process smears out (smoothes and biases) the 'true' model (i.e. that obtained using ordinary least-squares inversion without smoothing). If a diagonal element (denoted as r_{jj}) of the resolution matrix **R** is close to one, it indicates good model resolution at the corresponding loading point. In our inversion we find that the diagonal elements decrease to around zero at inland loading gridpoints far away from the deformation field. This is due to the fact that the loading response decreases with increasing distance between the loading and observing points. Inland points contribute negligibly to the deformation of the bedrock area, which lies ∼60 km and more away. In other words, the loading at these inland points is only weakly constrained by the deformation data. The inclusion of the $\lambda|\mathbf{Bu}|^2$ term in eq. (A4) strengthens the constraints on these inland points (in fact, on all points), by requiring their loading values to be similar to those of their neighbours. However, the strength of this requirement depends on the value we choose for λ. The inversion is unstable at inland points for small λ (e.g. $\lambda = 1$), but produces overly smoothed solutions at loading points near the InSAR deformation grid when λ is too large (e.g. $\lambda = 1 \times 10^3$).

To solve this problem, we allow λ to take on different values at different model points. We initially choose a large λ value (1×10^3), and calculate the resolution matrix **R** using eq. (A6). We then use the ratio between the minimum diagonal value ($r_{\min}$) and r_{jj} to scale λ at each model point, and minimize

$$S'' = \sum_{i=1}^{M}\left[d_i - \sum_{j=1}^{N} g_{i,j}u_j\right]^2 + \lambda\sum_{j=1}^{N}\frac{r_{\min}}{r_{jj}}\left[u_j - \frac{1}{4}\sum_{k=1}^{4}u_j^k\right]^2. \tag{A7}$$

Instead of eq. (A5), the solution to this new minimization problem is

$$\mathbf{u} = (\mathbf{G}^{\mathrm{T}}\mathbf{G} + \lambda\mathbf{F}\mathbf{B}^{\mathrm{T}}\mathbf{B})^{-1}\mathbf{G}^{\mathrm{T}}\mathbf{d}, \tag{A8}$$

where **F** is the scaling matrix for λ, whose off-diagonal elements are zero and the jth diagonal element is $r_{\min}/r_{jj}$. This method applies weaker smoothing at gridpoints near the deformation field and stronger smoothing over far-field gridpoints where the thinning is expected to be small. Therefore, this adaptive-smoothing method helps to further stabilize the solution, and to retain the high resolution in the near field where the thinning is expected to be large.